ADVANCED ELECTRONIC MATERIALS Open Access
www.advelectronicmat.de

Wearable Image-Based Colorimetric Sensor for Real-Time Gas Detection with High Chromaticity

*Ji-Eun Yeo, Joo Hwan Ko, Seung Hyeon Lee, and Young Min Song**

Flexible gas sensing technologies are essential for a wide range of environments and applications, from wearable devices to large-scale industrial systems. Among various approaches, colorimetric sensing stands out for its distinct advantages, including energy-free operation, intuitive visual feedback, and high resistance to environmental disturbances. Leveraging ultrathin resonators, colorimetric sensing achieves enhanced chromaticity and angular stability. In this study, a flexible colorimetric gas sensor is introduced based on a resonator array integrated with polyvinyl alcohol (PVA). This sensor achieves nearly 100% coverage of the standard RGB color gamut, enabling precise and visually distinguishable gas detection. Fabricated on a flexible substrate, it demonstrates remarkable angular robustness, maintaining consistent color under incident light angle variations of up to 60°. This capability, combined with rapid response times of 180 ms for PVA swelling and 210 ms for shrinking, highlights the sensor's adaptability for diverse applications, including wearable devices and industrial-scale monitoring. Furthermore, the sensor is evaluated under various volatile organic compounds (VOCs) and imaging conditions, showcasing its potential for image-based analysis and accurate VOC detection. Notably, it demonstrated the ability to detect VOC concentrations that are indistinguishable using a single sensor by simultaneously analyzing data from four sensor arrays.

1. Introduction

The ability to verify harmful gases in the environment is essential for detecting hazardous substances, preventing accidents, mitigating pollution, and ensuring public health and workplace safety. Developing wearable gas sensors that operate reliably under diverse conditions is critical for real-time monitoring. However, conventional gas verification methods face limitations in stability, energy efficiency, and adaptability to flexible surfaces. To overcome these challenges, various gas verification mechanisms, including chemiresistive, electrochemical, and optical-based approaches, are widely employed.[1] Among them, chemiresistive methods and electrochemical methods often require high operating temperatures for fast response times, making them susceptible to environmental disturbances.[2,3] Furthermore, integrating multiple sensing elements into a single array remains a significant challenge.[4] In contrast, optical-based gas sensing, particularly colorimetric sensors, offers distinct advantages, including zero-energy consumption, intuitive visual representation, and minimal susceptibility to external environmental influences.[5,6] These colorimetric sensors enable real-time imaging and analysis of gas-induced color changes using portable devices such as smartphones, facilitating rapid and accurate gas verification.[7] Despite these advantages, achieving high-performance colorimetric sensing requires a wide color gamut and long-term stability in color representation.[8]

From this perspective, structural coloration offers several crucial advantages over conventional pigment-based coloration.[9] Structural coloration can be found in various forms, including multilayer films,[10] bio-inspired designs,[11] photonic crystals,[12] and metasurfaces.[13] Conventional multilayer interferometers are predominantly based on Fabry–Perot (F-P) interference effects, enabling functionalities such as high-Q spectral characteristics and chromaticity.[14] The F-P resonance demonstrates a linear transition of the resonance wavelength;[15] however, its color representation is constrained, and the response time remains relatively slow.[16] Moreover, designs relying on F-P interference often exhibit pronounced angular sensitivity, leading to observable color shifts with changes in viewing angle. In contrast,

J.-E. Yeo, J. H. Ko, Y. M. Song
School of Electrical Engineering and Computer Science
Gwangju Institute of Science and Technology
Gwangju 61005, Republic of Korea
E-mail: ymsong@gist.ac.kr
S. H. Lee
School of Materials Science and Engineering
Gwangju Institute of Science and Technology
Gwangju 61005, Republic of Korea
Y. M. Song
Department of Semiconductor Engineering
Gwangju Institute of Science and Technology
Gwangju 61005, Republic of Korea
Y. M. Song
AI Graduate School
Gwangju Institute of Science and Technology
Gwangju 61005, Republic of Korea

The ORCID identification number(s) for the author(s) of this article can be found under https://doi.org/10.1002/aelm.202400977

DOI: 10.1002/aelm.202400977

ultrathin resonators composed of highly absorbent ultrathin films deposited on metal substrates selectively absorb incident light within the visible wavelength range, maintaining high color purity while offering excellent angular stability. The ultrathin resonators deliver consistent performance with minimal color shift, even at oblique angles, making them particularly well-suited for flexible and wearable applications.[17]

Recently, innovative approaches combining proteins[18] or hydrogels[6,11b,19] with simple photonic structures have been successfully demonstrated, leveraging their dynamic response to external stimuli. Compared to sensors utilizing a single cell, which are limited by a single resonance condition and exhibit reduced accuracy, arranging cells with multiple resonance conditions in an array allows for precise detection across a broader wavelength range.[21] Furthermore, this configuration enables eye-catching detection, which is visually distinguishable. This approach contributes to enhancing both detection performance and user convenience simultaneously. In this study, we present a flexible colorimetric sensor, based on a resonance array with multiple resonance conditions combined with polyvinyl alcohol (PVA). By leveraging these principles, we developed a gas sensor capable of covering 98.61% of the sRGB color gamut, demonstrating exceptional accuracy in color representation. This sensor array is fabricated on a flexible substrate using a thin-film photonic structure, allowing for versatile fabrication in terms of size and area. As a result, it can be miniaturized for attachment to curved surfaces, such as the human body, or applied to large-scale environments like factories where conspicuous detection is required. The sensor exhibits a rapid response time of 180 ms for swelling and 210 ms for shrinking. Furthermore, image-based analysis using array-based detection of volatile organic compound (VOC) gases demonstrated the sensor's ability to generate distinct color change patterns, enabling accurate gas detection. This capability highlights its potential as an efficient and practical gas sensing solution for precise VOC detection in diverse environments.

2. Results and Discussion

2.1. Wearable Gas Sensor with Multifunctional Color Code

Figure 1A presents an exploded view of a swelling layer-based colorimetric gas sensor integrated with a color-coded resonance array (CCRA). The active material was spin-coated onto a metal reflective layer and a porous lossy layer to form an ultrathin film. Fabricated on a flexible substrate, the sensor demonstrates exceptional adaptability, conforming seamlessly to various surfaces such as human skin or industrial components. The use of smartphone cameras for RGB data-based image analysis also offers a lightweight and cost-effective solution for field applications, providing high flexibility and portability while maintaining measurement accuracy through proper calibration.[22,23,25] Furthermore, its ultrathin structure facilitates integration into large-area applications (Figure 1B). The fabricated CCRA-based gas sensor (CCRA-GS) displays distinct colors depending on its resonant conditions, allowing real-time image-based analysis for the detection of not only humidity but also a range of VOCs such as acetone, isopropyl alcohol (IPA), and ethanol. The active layer, composed of PVA, expands or contracts in response to external environmental changes, directly coupling its physical deformation to the optical response and inducing immediate color changes within the CCRA-GS structure as the interference conditions are altered (Figure 1C).[26] This ultrathin architecture enhances colorimetric sensitivity through strong resonances at the interfaces of the CCRA, which possess complex optical constants. Notably, the hydrophilic nature of the fabricated sample enables distinct and visible color changes in response to variations in relative humidity (RH), demonstrating high sensitivity and clear visual outputs. This characteristic allows the sensor to modulate its color in accordance with RH fluctuations, without requiring any additional external energy input. These distinct color changes are attributed to sensitive resonance shifts of CCRA, resulting in strong resonance absorption at specific wavelengths, compared to other substrates such as Au, and Si (Figure S1, Supporting information).

Figure 1D presents the simulated electric field intensity profiles before and after the swelling of the PVA layer. The simulations were conducted at a wavelength of $\lambda = 430$ nm. A distinct standing wave pattern is observed when the PVA layer swells to a thickness of 400 nm. In contrast, when the PVA layer contracts to a thickness of 200 nm, the reflectance pattern weakens due to strong absorption at the specific wavelength. These results highlight the significant optical property changes in the CCRA structure, induced by the dimensional deformation of the PVA layer. The observed variations in the electric field distribution provide clear evidence of the sensitive resonance behavior within the structure. The photographic images presented in Figure 1E demonstrate distinct color changes across the visible spectrum under varying RH conditions, ranging from 20 to 90%. Each region exhibits different resonant conditions determined by the thickness of the lossy layer, resulting in diverse color variations across the regions. This observation effectively highlights the impact of detailed resonator structure design on color modulation characteristics. Moreover, leveraging diverse resonant conditions enables the realization of more eye-catching color changes than single-cell sensing, emphasizing its potential for enhanced sensing performance (Figure 1F). For instance, when the humidity increases from 20 to 90%, the region with $t_{Ge} = 70$ nm exhibits no noticeable color variation, whereas other cells display distinct color changes. However, within the narrow RH range of 80 to 90%, the corresponding region exhibits the most pronounced color change. These results indicate that arranging cells with different resonance conditions into an array enables multimodal sensing, facilitating detection across diverse environmental conditions or within specific RH ranges.

2.2. Optical Calculation of CCRA-GS

The cross sectional view of CCRA-GS is depicted in **Figure** 2A. The computational model incorporates a resonance structure consisting of a lossy medium and a metal reflector, coated with a swelling layer whose refractive index was determined experimentally (Figure S2, Supporting Information). The lossy medium can be implemented by modifying the porosity (P_r) of the highly absorbent material. In this study, the P_r of the Ge layer was precisely controlled by adjusting the deposition angle during thin-film deposition using the glancing angle deposition (GLAD) technique in E-beam evaporation. The porosity directly affects the

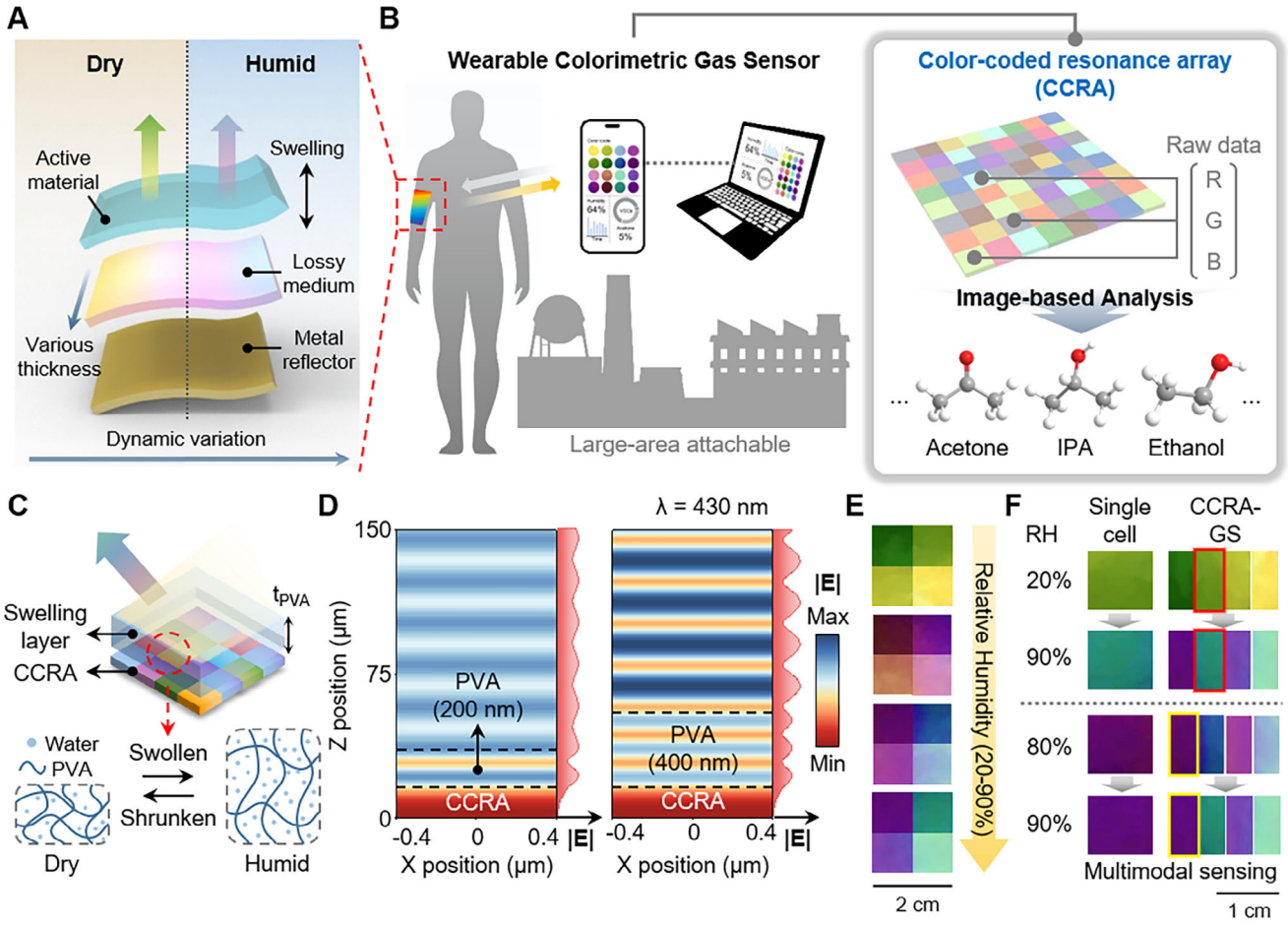

Figure 1. Wearable colorimetric gas sensor for image-based analysis. A) Exploded view of color-coded resonance array (CCRA)-based gas sensor (CCRA-GS) under the dry and humid state. B) Schematic illustration showing large-area attachable wearable colorimetric gas sensor and image-based gas detection analysis. C) Dimensional deformation of swelling layer (polyvinyl alcohol, PVA) due to swelling/shrinking mechanisms under changing humidity conditions. The CCRA exhibits different colors depending on the variation in the thickness of PVA (t_{PVA}). The Blue line and dot represent PVA network and water molecule, respectively. D) Simulated electric field at shrunken (t_{PVA} = 200 nm, left) and swelling (t_{PVA} = 400 nm, right) state. Optical simulation was conducted on a resonant structure consisting of 100 nm of Au and 50 nm of Ge at 430 nm wavelength. E) Measured color of CCRA-GS with varying relative humidity (RH) ranging from 20 to 90%. F) Multimodal sensing performance enabled by the CCRA under various RH variations. At RH level ranging from 20 to 90% (top), t_{Ge} = 70 nm region exhibits minimal color change, while the most pronounced response occurs within the narrower RH range of 80 to 90% (bottom).

effective refractive index and extinction coefficient, which can be described using the volume averaging theory (VAT) (Note S1, Supporting Information).[22] A multi-functional color code was realized by designing an array of resonant structures, each with distinct resonance conditions, achieved by shifting the resonance dip through controlled variations in the thickness of the lossy medium. In this model, the Ge layer functions as the lossy medium is deposited to a specified thickness of t_{Ge}, and the PVA layer, acting as the swelling layer, is sequentially spin-coated with t_{PVA}. For simulation purposes, we considered the refractive index of the background area as n = 1 (air). As shown in Figure 2B, the optimal resonance conditions can be identified by examining the contour map of reflectance as a function of the lossy layer's complex refractive index. Increasing P_r causes the system to shift closer to the resonance region, where the reflectance reaches its minimum. This signifies a critical point where light absorption is enhanced, enabling more sensitive color changes. By analyzing the reflectance spectra of Ge thin films with varying P_r, it was observed that as P_r increased from 10 to 70%, the intensity of the reflectance dip decreased, resulting in improved chromaticity (Figure 2C). Consequently, the ultra-thin layer structure of a Ge film with P_r 70%, paired with an Au reflector, was selected as the resonant structure (Figure S3, Supporting Information).

Figure 2D illustrates the RGB color sets corresponding to the spin-coated PVA layer with an initial expected thickness of 200 nm and a swelling thickness of 400 nm, as well as the color difference (ΔE) between these two states (see Note S2, Supporting Information). Significant color shifts with high contrast are observed near the resonance region marked by the white dashed line, which can be attributed to the reduction in reflectance caused by the increased P_r of the Ge layer. Figure 2E demonstrates the continuous shift of the reflectance dip with increasing PVA thickness. The reflectance dip, forming a 2nd-order resonance mode at approximately t_{PVA} = 200 nm, progressively

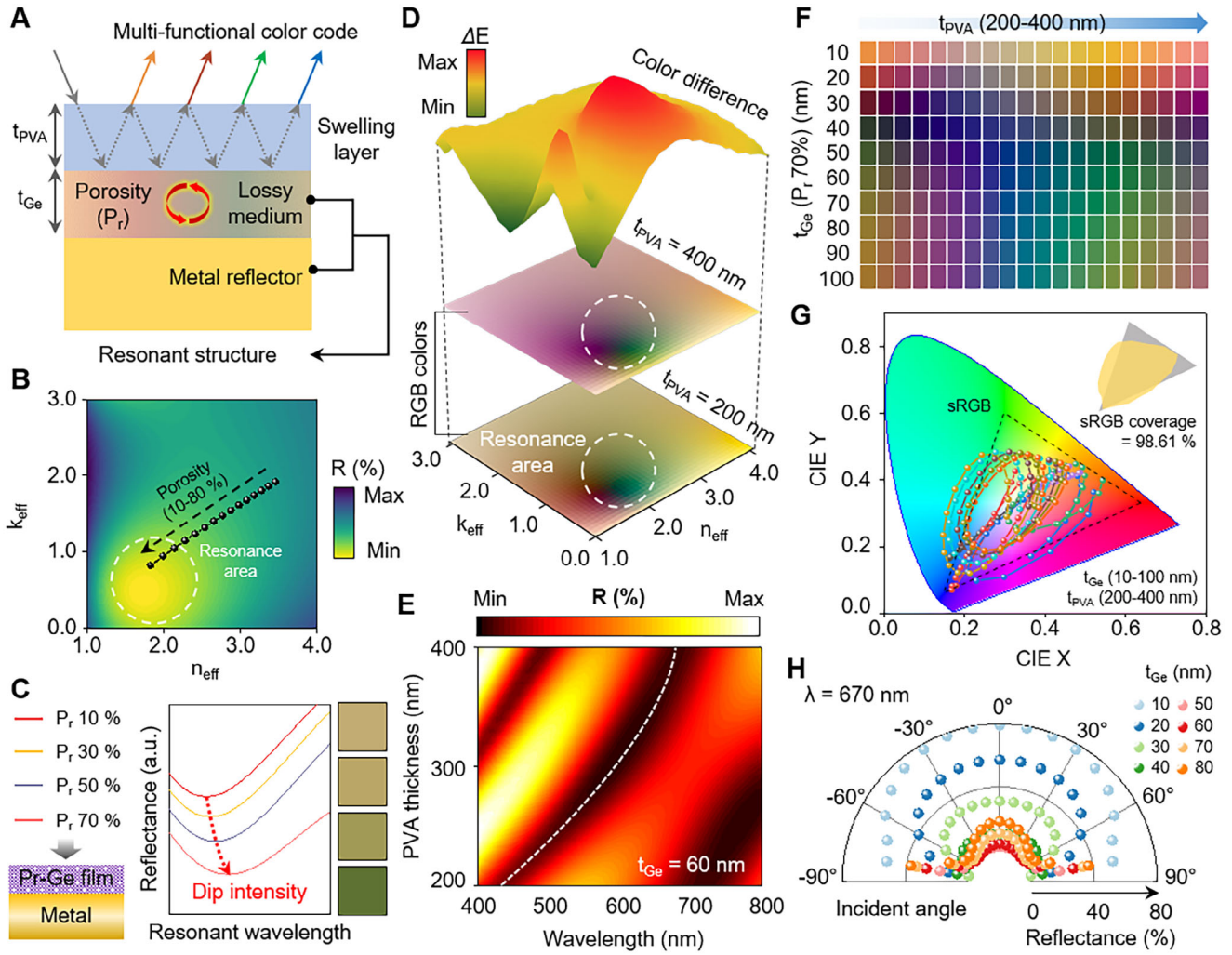

Figure 2. Structural and optical characterization of CCRA-GS. A) Schematic of a CCRA-GS, consisting of a porous-Ge (P_r-Ge) layer as a lossy medium, an Au reflector layer, and a PVA layer. The sensor features regions with varying Ge thickness (t_{Ge}) arranged in an array, showing multifunctional color codes in response to changes in the t_{PVA}. B) Complex refractive index coordinates with resonance area according to the various porosity of P_r-Ge. C) Simulated reflectance spectrum of CCRA (t_{Ge} = 60 nm, t_{PVA} = 200 nm) with various porosity conditions represent different dip intensities. D) RGB color representations and corresponding color differences (ΔE) with different PVA thickness (t_{PVA} = 200 nm / 400 nm) on the 2D surface of complex refractive index. E) Contour map of the calculated reflectance depending on dynamic change of swelling layer (P_r 70%, t_{Ge} = 60 nm). F) Color palette of various t_{Ge} according to dynamic change of t_{PVA}. G) CIE 1931 chromaticity diagram with simulated colors for the various values of PVA thickness. The dashed line represents the sRGB color gamut, with a coverage of 98.61% corresponding to changes in the t_{PVA} (inset). H) Calculated reflectance at λ = 670 nm corresponding to different incident angles and lossy layer thickness (t_{Ge} = 10 – 80 nm).

red-shifts as PVA swelling. To establish the resonance conditions for each cell in the CCRA, the wavelength positions of dip formation were analyzed for varying Ge layer thicknesses, along with the color changes resulting from PVA swelling. Figure 2F presents the color palette corresponding with the Ge layer thickness in resonant structures (P_r 70% Ge layer coated on Au metal layer), derived from conditions within the resonance region identified in previous results (Figure S4, Supporting Information). This palette emphasizes the Ge layer thickness-dependent color for implementing CCRA. If the metal layer is not strictly required to be Au, similar optical effects can still be achieved using alternative materials. For instance, metals such as Cu and Pt could potentially be employed, depending on the specific optical and physical properties desired for the application (Figure S5, Supporting Information). Furthermore, the achievable color gamut is compared with the sRGB color space in CIE coordinates, demonstrating that the chromaticity values dynamically shift across a wide range within the sRGB color space (Figure 2G).[23] The color variation resulting from changes in PVA thickness in resonant structures with different Ge layer thicknesses covers 98.61% of the sRGB color space, suggesting that the color distribution can dynamically span nearly the entire sRGB gamut (Figure S6, Supporting Information). The wide sRGB coverage enables the detection of subtle color variations across a broad range, making it particularly beneficial for applications such as health monitoring and environmental sensing. Furthermore, the sensor's angular robustness enables stable colorimetric responses on curved surfaces like skin or textiles, ensuring reliable performance in

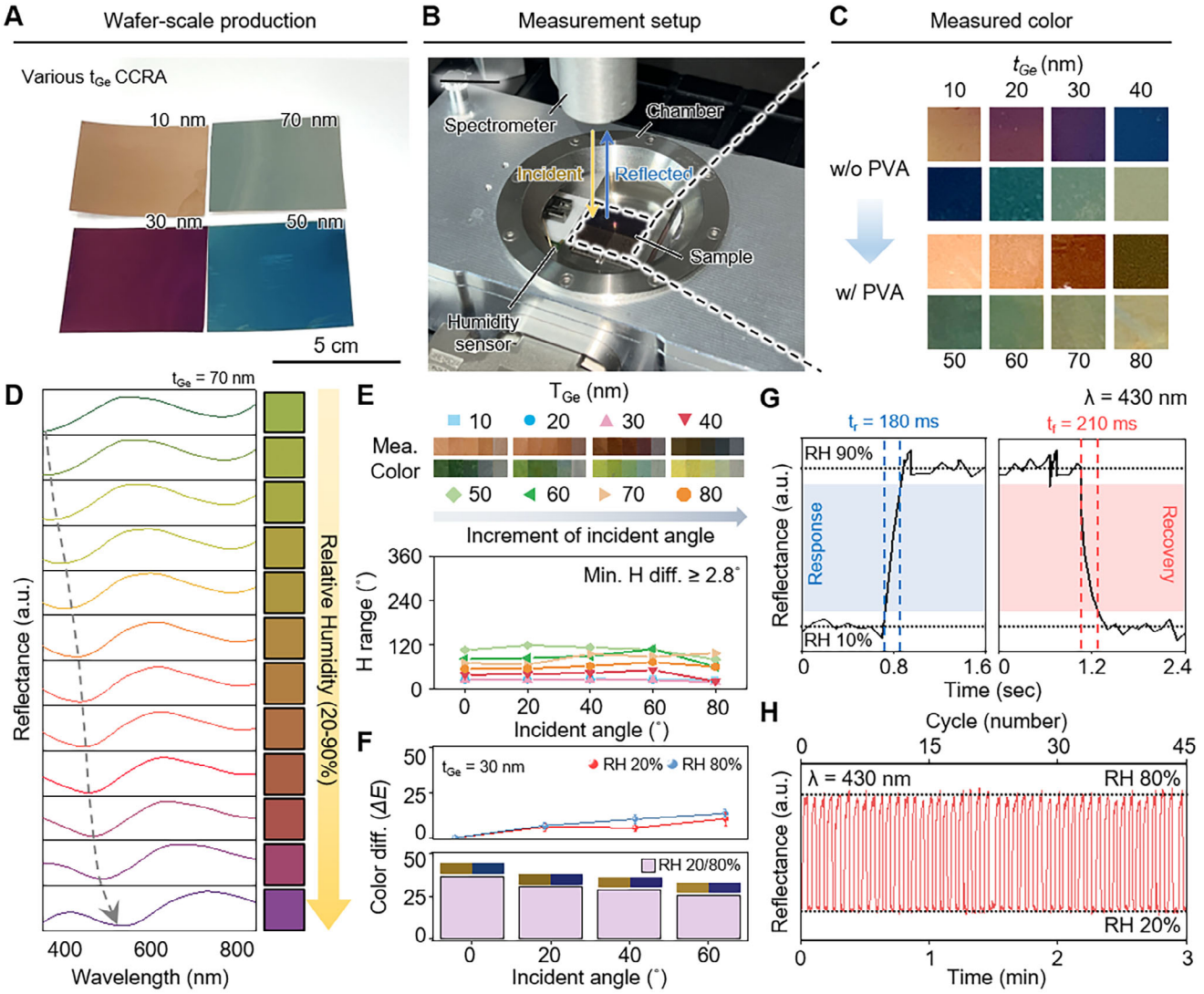

Figure 3. Experimental evaluation of sensing and color performance. A) Photograph of wafer-scale CCRA-GS with varying t_{Ge}. B) Measurement setup for real-time reflectance analysis under controlled humidity conditions and the scale bar is 2 cm. C) Experimentally measured color palette before and after PVA coating for different t_{Ge}. D) Reflectance spectra measured within the wavelength range from 400 – 800 nm at t_{Ge} = 70 nm under RH levels ranging from 20 to 90%. E) Hue range comparison with respect to the light incident angle (0° to 80°) across cells with different t_{Ge}. Experimentally measured colors (top) and Hue range variations (bottom). F) ΔE values attributed to the changes in the light incident angle (top) and humidity-induced color variations (bottom) at RH 20 and 80%. G) Response and recovery times for RH transitions from 10 to 90%, determined via reflectance intensity at $\lambda = 430$ nm. H) Repeatability analysis, conducted by monitoring reflectance intensity at $\lambda = 430$ nm during cyclic RH variations between 20 and 80%. Each RH state was maintained for 5 s and repeated for more than 45.

wearable applications without precise optical alignment. The calculated reflectance values as a function of the incident angle at λ = 670 nm are presented in Figure 2H, enabling an analysis of the reflectance characteristics with varying incident angles. Due to the difficulty in observing reflected colors at extreme incident angles, simulations were conducted within the 0–80° range (Figure S7, Supporting Information). Comparison based on the Ge layer thickness reveals that similar colors are maintained at incident angles above 60° for thicknesses in the range of 10–40 nm and above 40° for thicknesses in the range of 50–80 nm at t_{PVA} = 200 nm (Figure S8, Supporting Information). It is also observed that even with the color change induced by PVA swelling, the color remains consistent up to an incident angle of 40° at every condition (Figure S9, Supporting Information).

2.3. Experimental Humidity Sensing and Performance Evaluation

Figure 3A illustrates the wafer-scale fabrication of the CCRA with varying Ge layer thicknesses. For large-area fabrication, the PVA layer was deposited via spin-coating (Figure S10, Supporting Information). To evaluate the humidity detection and coloration performance of the CCRA-GS, the experimental measurement setup has been implemented to observe real-time color change

in response to humidity variation, as shown in Figure 3B (Figure S11, Supporting Information). Water vapor and N_2 gas are introduced into the tube to control the RH level within the measurement chamber, where water vapor increases RH, and N_2 gas decreases it. The real-time monitoring of temperature and humidity was performed using a commercial sensor. By comparing the measured color changes as a function of Ge layer thickness in the CCRA-GS before and after PVA coating with simulation results, the expected thicknesses of each layer and the refractive index of PVA can be determined (Figure 3C). The measured reflectance spectra corresponding to the RH variation from 20 to 90% are shown in Figure 3D. To prevent water condensation on the chamber glass, the maximum RH was limited to 90%. The measured reflectance dip at $t_{Ge} = 70$ nm exhibits a redshift as RH increases from 20 to 90%; green, orange to purple color changes can be observed.[17]

To evaluate angle robustness, the color variation with increasing incident light angles was examined under RH 30% conditions for each cell ($t_{Ge} = 10$–80 nm). Due to the minimal reflected light intensity at 90°, which made color observation challenging, the measurements were restricted to an incident angle range of 0° to 80°. The top panel of Figure 3E presents the experimentally measured colors for each region, while the bottom panel illustrates the changes in the Hue range corresponding to the variation in the incident angle. The observed color variation ranged from a minimum of 2.8° ($t_{Ge} = 10$ nm) to a maximum of 48° ($t_{Ge} = 60$ nm), indicating minimal hue changes across the measured range. These results confirm that the structure exhibits strong angle robustness within the incident angle range of 0° to 80°, effectively maintaining consistent color properties under varying optical conditions. Each region's color palette as a function of the incident angle, along with the ΔE values calculated based on RGB data, is presented in Figure S12 (see Supporting Information). Furthermore, to assess the angle dependence and active characteristics under humidity variations, the color difference resulting from humidity changes was calculated based on the measured data for each incident angle and presented with standard deviation values in Figure 3F. In the $t_{Ge} = 30$ nm cell, ΔE were compared under RH 20 and 80% conditions while varying the incident angle. While the color remained consistent across the measured angles, the ΔE values before and after the humidity change demonstrated that the humidity sensing properties are still preserved, even when optical conditions change.

To quantitatively evaluate the sensing characteristics of the CCRA-GS, response time and repeatability were measured. The response and recovery times were determined by examining the intensity variations in the reflectance spectrum at a single wavelength ($\lambda = 430$ nm) and are characterized as the duration required to reach 10–90% of the intensity difference between equilibrium states (Figure 3G). The optical resonant structure, integrated with the active material, demonstrates rapid activation within 180 ms (response) as the RH increases from 10 to 90%, and efficiently restores to its initial state within 210 ms (recovery). This performance is attributed to the strategic placement of the active PVA layer on the uppermost surface, which enhances water molecule diffusion and accelerates the reaction kinetics. Additionally, repeatability tests were conducted to assess whether the sensor consistently provides accurate sensing results under the same conditions. This was verified through cyclic experiments with RH varying between 20 and 80%. As shown in Figure 3H, the reflectance intensity at 430 nm was consistently achieved and recovered over more than 45 cycles. These results demonstrate the quantitative analysis of the response characteristics and stability of the CCRA-GS. In addition, the sensor exhibited consistent response and recovery times throughout 45 cycles of humidity switching, demonstrating excellent stability and reliability under repeated operation cycles (Figure S13, see Supporting Information).

2.4. Gas Verification Performance and Imaging Condition Stability under Variable Conditions

The gas verification process based on image-based analysis of CCRA-GS is effectively demonstrated in **Figure 4A**. Instead of utilizing VOC-selective materials, the CCRA-GS employs a single material arranged in an array format to differentiate responses to various VOCs. This array-based configuration allows for color coding of VOC responses, eliminating the need for complex material synthesis and reducing optical structural complexity. The characteristics of various colorimetric sensors based on humidity and existing sensors utilizing different gas detection methods are presented in Tables S1 and S2, respectively.[32–34] CCRA-GS consists of four gas-sensitive pixels and four reference pixels that are insensitive to gases. The reference pixels serve as control points, enabling quantitative evaluation of the sensor's color change after gas exposure. For concentration-dependent color measurements, ethanol, methanol, IPA, and acetone liquids were vaporized using a heater to reach the target concentrations. The VOC gas concentration was calculated based on the complete evaporation of the liquid phase, applying the ideal gas law to determine the gas concentration using temperature, pressure, and volume. This method enables precise control of VOC levels without requiring additional reference sensors (see Experimental Section and Note S3, Supporting Information). All measurements were conducted under identical illumination conditions in the enclosed chambers. A white background was used to block reflected light from surrounding objects, ensuring uniform reflection from the sample. Additionally, to eliminate any influence of natural light in the laboratory, all experiments were performed under a stable LED light source. Each gas-sensitive pixel region has a unique resonance wavelength, and distinct color responses, depending on the concentration and specific VOC type, resulting in different datasets. The captured image datasets were converted to the average RGB values of the pixel regions, and by analyzing these values, specific patterns were identified. Average RGB values reduce pixel-level variations, ensuring a more stable and reliable representation of color changes. Figure 4B presents a color palette that visually compares the pixel colors at different concentrations of each VOC. The pixel array configuration is as follows: i) $t_{Ge} = 50$ nm, ii) $t_{Ge} = 60$ nm, iii) $t_{Ge} = 70$ nm, and iv) $t_{Ge} = 80$ nm. Depending on the type and concentration of the VOC, each region exhibits distinct colors. The ΔE between the control pixel and the average RGB values of each region was calculated and analyzed through image-based analysis, resulting in the formation of identification patterns (Figure S14, Supporting Information). Figure 4C visually illustrates the identification patterns derived from the combination of regional color responses to various

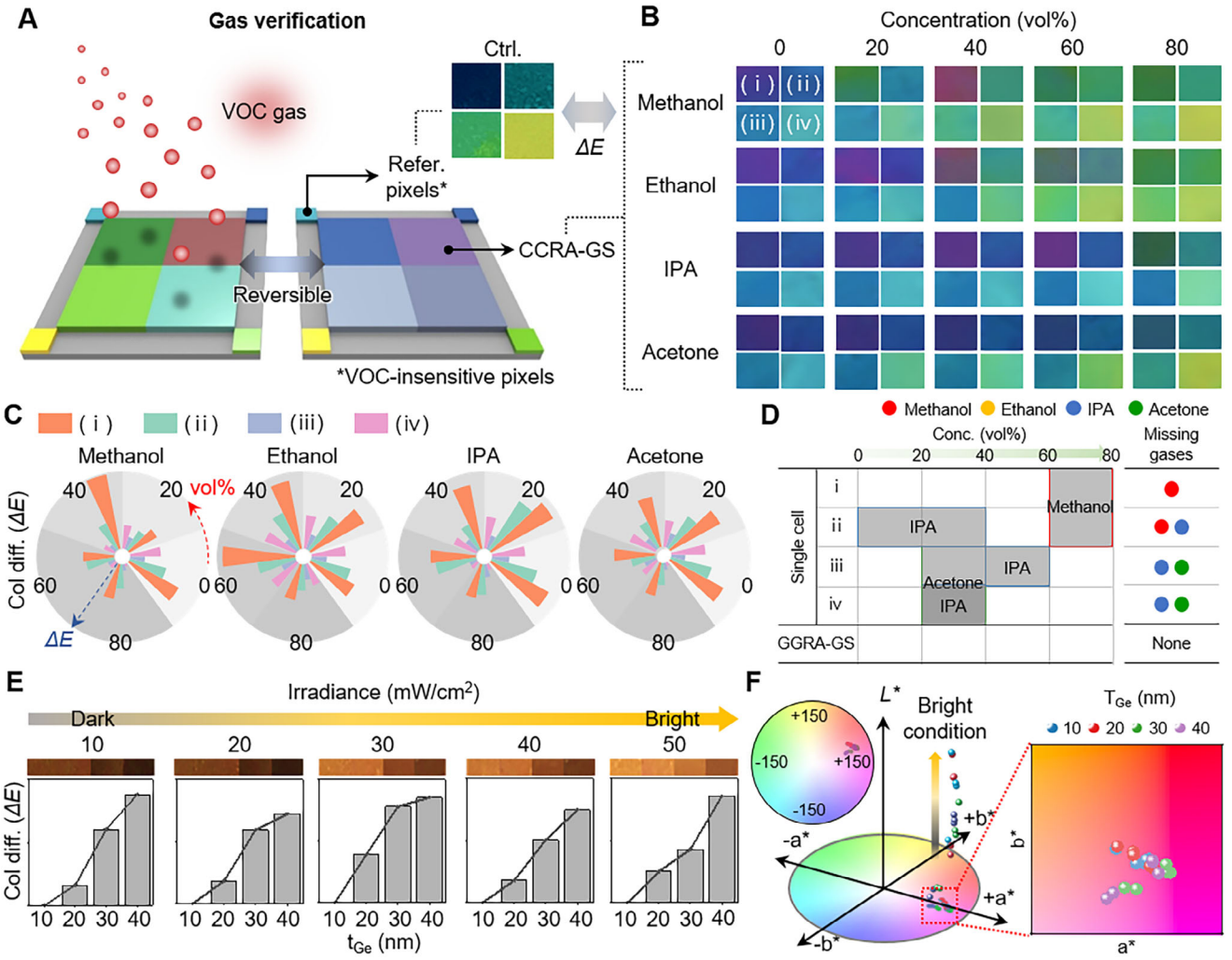

Figure 4. Gas verification and imaging condition stability performance. A) Schematic representation of CCRA-GS for VOC gas verification with four segmented sensor arrays. VOC-insensitive pixels are designated as reference pixels, serving as control pixels to provide a baseline for calculating color changes. B) Color palettes correspond to varying concentrations of different VOC types, including methanol, ethanol, isopropyl alcohol (IPA), and acetone. C) ΔE of the CCRA-GS corresponds to variations in the type and concentration of chemical substances, enabling their use as fingerprint patterns. D) Blind spots and missing gasses for each VOC gas concentration during single cell and CCRA-GS operation. Blind spots were defined as points where the $\Delta E \leq 2.5$, calculated from color changes induced by VOC concentration variations. E) Imaging condition stability evaluation through ΔE observed across different cell regions under various irradiation conditions for evaluating the outdoor sensing capabilities of the CCRA-GS. F) The corresponding 3D CIELAB coordinates are derived from the RGB values of the captured images under various irradiation conditions.

substances. Distinct characteristics are observed for different VOC gases, including methanol, ethanol, IPA, and acetone. CCRA-GS induces unique color change patterns for each VOC, providing crucial information for distinguishing between them. Due to its operation across a broad wavelength range, CCRA-GS offers the advantage of generating identification patterns for a variety of gases. To highlight the potential of deep learning in this sensor for colorimetric film interpretation and classification, the hierarchical clustering analysis (HCA) of ΔRGB intensity changes for different VOCs at varying concentrations, demonstrating the sensor's ability to quantitatively classify gas types and concentrations (Figure S16, Supporting Information). Furthermore, these sensors can provide superior accuracy compared to single cell operation. Figure 4D analyzes the blind spots and missing gases according to VOC gas concentrations that occur during operation in a single cell mode and CCRA-GS. A blind spot is defined as a point where the color change calculated from the gas concentration variation results in a ΔE value of 2.5 (Figure S15, Supporting Information). At these points, the color difference due to concentration changes is visually indistinguishable, suggesting that accurate detection may be challenging with a single cell system.[25] Furthermore, since these regions occur at different pixels and concentration ranges for each gas. For instance, i) pixel can detect IPA across the entire concentration range but is unable to detect methanol in the 60–80 vol.% range. In contrast, iii) pixel can detect methanol across the entire concentration range but fails to detect acetone and IPA within the 20–40 and 40–60 vol% ranges, respectively. To address these limitations, the CCRA-GS compensates for them by utilizing relative color change data

from surrounding pixels, thereby acquiring diverse datasets and improving accuracy. This result highlights the potential of the sensor for selective VOC detection based on optical signal patterns. This approach can be more precisely implemented through a dynamic compensation mechanism that considers the nonlinear response characteristics and color change sensitivity to gas concentrations. By quantifying the frequency and magnitude of blind spot occurrences and compensating for the limited response characteristics of the single cell system, it has the potential to reduce blind spots and enhance overall detection capabilities.

Ensuring the successful application of the proposed flexible gas sensor in wearable devices or large-area industrial environments requires more than just a focus on high chromaticity, angle robustness, and gas selectivity through image-based analysis. Alongside these considerations, it is equally essential for the sensor to maintain stability and reliable performance under a range of fluctuating environmental conditions, such as those encountered in outdoor settings. These include variations in ambient lighting, temperature shifts, and other atmospheric factors, all of which can influence sensor accuracy. Therefore, achieving environmental stability is crucial for ensuring that the sensor delivers consistent and accurate results in real-world applications. To evaluate this, the CCRA-GS was exposed to varying irradiance conditions, and distinct color variations were observed across different regions under each condition (Figure 4E). For a quantitative comparison of chromatic analysis, we converted the RGB values of the captured image to the CIELAB color space, as shown in Figure 4F (Note S2, see Supporting Information). The results revealed that under bright conditions, the L value, which represents lightness, increased, while the a and b values, which represent color components, remained nearly constant as depicted in the 2D view of the CIELAB space. This indicates that as brightness increases, the primary change occurs in the lightness of the color, with minimal variation in hue. By analyzing the color variations, we assessed how the sensor responds to fluctuations in irradiance, suggesting that it can maintain consistent color characteristics across different environmental conditions, which provides a solid basis for ensuring stable performance in outdoor environments. Furthermore, the CCRA-GS demonstrates its potential for wearable applications by maintaining its structural integrity and color stability when attached to a human wrist and subjected to mechanical deformation, highlighting its flexibility and conformability (Figure S17, Supporting Information).

3. Conclusion

In conclusion, we demonstrated a wearable gas sensor by integrating a PVA layer with a resonator array composed of Au reflector and P_r-Ge lossy medium. The sensor, fabricated on a flexible substrate, exhibits high chromaticity, covering over 98% of the sRGB color gamut, along with superior angular stability enabled by the ultrathin resonator design. These attributes highlight the sensor's suitability for diverse applications, including curved surfaces such as human skin and large-scale industrial environments. The proposed sensor leverages a simple resonant structure and a PVA spin-coating process, enabling large-area fabrication. It demonstrates rapid dynamic response and sensitive colorimetric behavior due to significant curvature changes induced by PVA swelling. The resonance region was optimized by considering the complex refractive index variation. When the RH was modulated between 20% and 90%, a single pixel was shown to generate green, orange, and purple colors. The colorimetric sensor pixels are arranged in an array with distinct resonant wavelengths, allowing for the identification of detection patterns that are more prominent compared to single-cell sensing, thereby enabling high-resolution detection of VOC gases through integrated image-based analysis. This approach provides a reliable and visually intuitive gas verification capability. The sensor's simple fabrication, relying only on thin-film deposition, highlights its scalability. Additionally, potential enhancements to the PVA layer, such as nanocomposite fillers, cross-linking, hybrid blends, and structural frameworks, could further improve long-term stability for real-world applications.[27–30] The proposed solution is practical, energy-efficient, and scalable, offering a promising pathway for applications in wearable devices and industrial safety systems.

4. Experimental Section

Optical Calculation: The optical characterization of the CCRA-GS was conducted using the rigorous coupled-wave analysis (RCWA) method implemented in commercial software (Diffract MOD, RSoft Design Group, USA). The complex refractive indices of Ge and Au were obtained from the literature,[31] while the complex refractive index of PVA was measured using an ellipsometer (Elli-SEUN-am8, Ellipso Technology Co., Ltd., South Korea) on a 200 nm thin film deposited from a 4 wt.% PVA solution at 2000 rpm for 60 s. The effective complex refractive indices, accounting for porosity, were calculated based on the volumetric averaging theory (VAT) using MATLAB (MathWorks, Inc.).[22a] All simulation results were ensured to maintain numerical stability and high precision by incorporating a diffraction order up to the ninth and employing a grid spacing of 1 nm.

Fabrication of CCRA-GS: To fabricate the CCRA, a PET substrate was selected to ensure flexibility. The substrate was cleaned through ultrasonic treatment in acetone, IPA, and DI water for 5 min each. Subsequently, under high vacuum conditions ($\approx 10^{-6}$ Torr), an Au layer was deposited as a metallic reflector with a thickness of 100 nm using a magnetron radio-frequency sputtering system (DDHT-LSH2, Daedong Hi-Tech, South Korea). To achieve a porous medium, a Ge layer (lossy medium) was prepared via GLAD method under high vacuum ($\approx 10^{-6}$ Torr). Deposition was performed using an electron beam evaporation system (KVEE2000, Korea Vacuum Tech Co., South Korea). A custom-tilted sample holder mounted with a flexible Au film was used, and the Ge layer was deposited at a controlled rate of ≈ 1 Å s^{-1} to achieve the desired thickness (t_{Ge} = 10–80 nm). For the PVA coating layer, a 4 wt.% PVA solution was prepared by dissolving commercial PVA granular particles (Sigma-Aldrich Co., USA) in DI water and stirring overnight at 90 °C. The prepared PVA solution was then spin-coated onto the CCRA at 2000 rpm for 60 s to form the PVA layer.

Humidity-Responsive Optical Characteristic: The humidity-responsive reflectance spectra were measured under normal incidence using a custom-designed chamber equipped with a humidity sensor and a spectrometer (OCEAN-HDX-VIS-NIR, Ocean Insight, USA). The RH within the chamber was controlled by adjusting the flow rate of N2 saturated with water vapor, defined by the input and exhaust flow rates. A Xe lamp (SLS400, Thorlabs, USA), connected via an optical fiber, was employed as the light source, and only the reflected light was captured through the optical fiber and detected by the spectrometer. A transparent glass window was placed between the sample and the measurement fiber, and the background reflectance, including the glass's reflection effects, was also measured.

VOC Measurement of CCRA-GS: CCRA-GS was employed to monitor the colorimetric response to VOCs. The CCRA comprised four distinct sensing regions, where PVA films responded to VOC vapor by swelling, inducing noticeable color changes. The required liquid volume for each VOC

was calculated based on the ideal gas law (Note S3, Supporting Information). The CCRA-GS was mounted inside a closed chamber with a horizontally fixed sample holder. The chamber temperature was maintained constant using a heater, ensuring uniform evaporation of VOCs. The VOC vapors were generated in the chamber, and real-time color changes of the CCRA were recorded using a camera. The evaporation rate of VOCs remained consistent due to the controlled temperature and fixed evaporation surface.[24] To analyze the colorimetric changes, the time required for color saturation was divided into intervals of 20%, and the color evolution was evaluated over time. After each VOC measurement, the chamber was purged with N_2 to remove any residual VOCs, restoring the system for subsequent measurements.

Supporting Information

Supporting Information is available from the Wiley Online Library or from the author.

Acknowledgements

This work was supported by the National Research Foundation of Korea(NRF) grant funded by the Korea government (MSIT) (RS-2023-NR077254 and RS-2021-NR057359). This material was also supported by the Technology Innovation Program (RS-2024-00467230, Development of a Digital Healthcare Device for Non-invasive Continuous Monitoring of Myocardial Infarction Biomarkers Based on Mid-Infrared Nano-Optical Filters) funded by the Ministry of Trade Industry & Energy (MOTIE, Korea)

Conflict of Interest

The authors declare no conflict of interest.

Data Availability Statement

The data that support the findings of this study are available from the corresponding author upon reasonable request.

Keywords

color-coded array, colorimetric sensor, outdoor environment detection, structural color, thin-film coloration, VOC detection

Received: December 27, 2024
Revised: March 6, 2025
Published online: April 10, 2025

[1] S. Y. Jeong, J. S. Kim, J. H. Lee, *Adv. Mater.* **2020**, *32*, 2002075.
[2] S.-J. Choi, I. Lee, B.-H. Jang, D.-Y. Youn, W.-H. Ryu, C. O. Park, I.-D. Kim, *Anal. Chem.* **2013**, *85*, 1792.
[3] A. H. Jalal, F. Alam, S. Roychoudhury, Y. Umasankar, N. Pala, S. Bhansali, *ACS Sens* **2018**, *3*, 1246.
[4] a) H. Kang, S. Y. Cho, J. Ryu, J. Choi, H. Ahn, H. Joo, H. T. Jung, *Adv. Funct. Mater.* **2020**, *30*, 2002486; b) L. Spinelle, M. Gerboles, G. Kok, S. Persijn, T. Sauerwald, *Sensors* **2017**, *17*, 1520; c) F. Xu, W. Li, S. Sun, A. Zhong, X. Cheng, J. Shi, Z. Li, J. Li, W. Zhang, X. Wang, *ACS Appl. Nano Mater.* **2023**, *6*, 8335.
[5] S. H. Nah, J. B. Kim, H. N. T. Chui, Y. Suh, S. Yang, *Adv. Mater.* **2024**, *36*, 2409297.
[6] H. J. Nam, J. H. Ko, H. E. Jeong, Y.-W. Oh, S. Jung, I.-S. Kang, Y. M. Song, G. J. Lee, *Optica* **2024**, *11*, 1425.
[7] R. E. Owyeung, M. J. Panzer, S. R. Sonkusale, *Sci. Rep.* **2019**, *9*, 5607.
[8] a) N. Jarulertwathana, S. Mohd-Noor, J. K. Hyun, *ACS Appl. Mater. Interfaces* **2021**, *13*, 44786; b) H. Chi, Y. J. Liu, F. Wang, C. He, *ACS Appl. Mater. Interfaces* **2015**, *7*, 19882.
[9] a) Z. Xuan, J. Li, Q. Liu, F. Yi, S. Wang, W. Lu, *Innovation* **2021**, *2*, 100081; b) C. Jung, G. Kim, M. Jeong, J. Jang, Z. Dong, T. Badloe, J. K. Yang, J. Rho, *Chem. Rev.* **2021**, *121*, 13013.
[10] a) J. H. Han, D.-Y. Kim, D. Kim, K. C. Choi, *Sci. Rep.* **2016**, *6*, 29341; b) J. H. Ko, S.-H. Hong, S.-K. Kim, Y. M. Song, *Iscience* **2023**, *26*, 105780; c) J. H. Ko, J. H. Park, Y. J. Yoo, S. Chang, J. Kang, A. Wu, F. Yang, S. Kim, H. G. Jeon, Y. M. Song, *Adv. Sci.* **2023**, *10*, 2304310; d) J. H. Ko, Y. J. Yoo, Y. Lee, H.-H. Jeong, Y. M. Song, *IScience* **2022**, *25*, 104727.
[11] a) H. Fudouzi, *Sci. Technol. Adv. Mater.* **2011**, *12*, 064704; b) M. Qin, M. Sun, R. Bai, Y. Mao, X. Qian, D. Sikka, Y. Zhao, H. J. Qi, Z. Suo, X. He, *Adv. Mater.* **2018**, *30*, 1800468; c) J. H. Ko, J.-E. Yeo, H. E. Jeong, H. M. Kim, Y. J. Yoo, Y. Yuk, S. Lee, Y. M. Song, *Biosens. Bioelectron.* **2024**, *260*, 116445.
[12] a) Y. Y. Diao, X. Y. Liu, G. W. Toh, L. Shi, J. Zi, *Adv. Funct. Mater.* **2013**, *23*, 5373; b) Y. Shen, V. Rinnerbauer, I. Wang, V. Stelmakh, J. D. Joannopoulos, M. Soljacic, *ACS Photonics* **2015**, *2*, 27.
[13] a) C. Jung, Y. Yang, J. Jang, T. Badloe, T. Lee, J. Mun, S.-W. Moon, J. Rho, *Nanophotonics* **2020**, *10*, 919; b) Y. Xu, Y. Wang, Y. Yang, S. Yang, L. Li, R. Xiang, J. Liu, *Opt. Express.* **2024**, *32*, 6776; c) J. H. Ko, J.-E. Yeo, H. E. Jeong, D. E. Yoo, D. W. Lee, Y.-W. Oh, S. Jung, I.-S. Kang, H.-H. Jeong, Y. M. Song, *Nanophotonics* **2024**, *13*, 1119.
[14] a) A. Kumar, D. Pawar, D. J. Late, R. Kanawade, *J. Mater. Sci.: Mater. Electron.* **2022**, *33*, 2509; b) R. Kanawade, A. Kumar, D. Pawar, D. Late, S. Mondal, R. K. Sinha, *JOSA B* **2019**, *36*, 684; c) R. Kanawade, A. Kumar, D. Pawar, K. Vairagi, D. Late, S. Sarkar, R. K. Sinha, S. Mondal, *Opt. Express.* **2019**, *27*, 7277.
[15] a) J. Jang, K. Kang, N. Raeis-Hosseini, A. Ismukhanova, H. Jeong, C. Jung, B. Kim, J. Y. Lee, I. Park, J. Rho, *Adv. Opt. Mater.* **2020**, *8*, 1901932; b) D. Ghindani, I. Issah, S. Chervinskii, M. Lahikainen, K. Kuntze, A. Priimagi, H. Caglayan, *ACS Photonics* **2022**, *9*, 2287; c) D. H. Kim, Y. J. Yoo, J. H. Ko, Y. J. Kim, Y. M. Song, *Opt. Mater. Express* **2019**, *9*, 3342.
[16] A. G. Erlat, M. Yan, A. R. Duggal, in *Flexible Electronics. Electronic Materials: Science & Technology*, (Eds: W. S. Wong, A. Salleo), Springer, Boston, MA **2009**, p. 413.
[17] a) M. A. Kats, R. Blanchard, P. Genevet, F. Capasso, *Nat. Mater.* **2013**, *12*, 20; b) D. H. Seo, S.-Y. Heo, Y. M. Song, G. J. Lee, *IEEE Photonics J.* **2022**, *14*, 0618006.
[18] a) Y. J. Yoo, W. G. Kim, J. H. Ko, Y. J. Kim, Y. Lee, S. G. Stanciu, J. M. Lee, S. Kim, J. W. Oh, Y. M. Song, *Adv. Sci.* **2020**, *7*, 2000978; b) Z. Wang, J. H. Lee, Y. Lu, *Adv. Mater.* **2008**, *20*, 3263.
[19] Y. Zhao, Z. Xie, H. Gu, C. Zhu, Z. Gu, *Chem. Soc. Rev.* **2012**, *41*, 3297.
[20] B. Ko, J. Kim, Y. Yang, T. Badloe, J. Park, J. H. Ko, M. Jeong, H. Kang, C. Jung, Y. M. Song, *Adv. Sci.* **2023**, *10*, 2204469.
[21] J. Jia, S. Zhang, L. Ma, L. Zheng, S. Yu, C. Shen, H. Fu, S. Wang, Y. She, *Sci. Rep.* **2022**, *12*, 18596.
[22] a) A. Garahan, L. Pilon, J. Yin, I. Saxena, *J. Appl. Phys.* **2007**, *101*, 014320; b) J. H. Ko, Y. J. Yoo, Y. J. Kim, S. S. Lee, Y. M. Song, *Adv. Funct. Mater.* **2020**, *30*, 1908592.
[23] N. Ohta, A. Robertson, *Colorimetry: Fundamentals and Applications*, John Wiley & Sons, Hoboken, NJ **2006**.
[24] D. W. Oxtoby, H. P. Gillis, L. J. Butler, *Cengage AU* **2016**.
[25] M. D. Fairchild, *Color Appearance Models*, John Wiley & Sons, Hoboken, NJ **2013**.
[26] H. Hu, X. Zhang, Y. He, Z. s. Guo, J. Zhang, Y. Song, *J. Appl. Polym. Sci.* **2013**, *130*, 3161.

[27] M. Zouari, S. G. Stanciu, J. Jakes, L. Marrot, E. Fiorentis, G. A. Stanciu, D. B. DeVallance, *J. Mater. Res. Technol.* **2023**, *27*, 5533.
[28] S. Kashyap, S. K. Pratihar, S. K. Behera, *J. Alloys Compd.* **2016**, *684*, 254.
[29] R. V. Gadhave, S. Vineeth, P. T. Gadekar, *J. Mater. Environ. Sci.* **2020**, *11*, 704.
[30] J. Sringam, P. Pankongadisak, T. Trongsatitkul, N. Suppakarn, *Polymers* **2022**, *14*, 3552.
[31] a) D. L. Windt, W. C. Cash Jr, M. Scott, P. Arendt, B. Newnam, R. Fisher, A. Swartzlander, *Appl. Opt.* **1988**, *27*, 246; b) D. E. Aspnes, A. Studna, *Phys. Rev. B* **1983**, *27*, 985.
[32] K. Iitani, P.-J. Chien, T. Suzuki, K. Toma, T. Arakawa, Y. Iwasaki, K. Mitsubayashi, *ACS Sens* **2018**, *3*, 425.
[33] I. D. Kim, S. J. Choi, S. J. Kim, J. S. Jang, *Smart Sens. Health Environ. Monitor.* **2015**, 19.
[34] K.-I. Choi, H.-J. Kim, Y. C. Kang, J.-H. Lee, *Sens. Actuators, B* **2014**, *194*, 371.